Progress in Natural Science: Materials International 31 (2021) 688–697

HOSTED BY

Contents lists available at ScienceDirect

Progress in Natural Science: Materials International

journal homepage: www.elsevier.com/locate/pnsmi

Original Research

Corrosion resistance and thermal stability of sputtered $Fe_{44}Al_{34}Ti_7N_{15}$ and $Al_{61}Ti_{11}N_{28}$ thin films for prospective application in oil and gas industry

Mahbub Alam Maruf [a], Syed Muhammad Mujtaba Rizvi [a], Mohammed Noor-A-Alam [b], Donghyun Shin [a], Waseem Haider [a], Ishraq Shabib [a,*]

[a] School of Engineering and Technology, Central Michigan University, Mt. Pleasant, MI, 48859, USA
[b] Mechanical Engineering, Indiana University-Purdue University Columbus, Columbus, IN, 47203, USA

ARTICLE INFO

Keywords:
Thin films
Metallic glasses
X-ray diffraction
Photoelectron spectroscopy
Corrosion
Thermal analysis

ABSTRACT

Fe-and Al-based thin-film metallic glass coatings ($Fe_{44}Al_{34}Ti_7N_{15}$ and $Al_{61}Ti_{11}N_{28}$) were fabricated using magnetron co-sputtering technique, and their corrosion performances compared against wrought 316L stainless steel. The results of GI-XRD and XPS analyses demonstrated amorphous structure and oxide layer formation on the surface of the fabricated thin films, respectively. The potentiodynamic (PD) polarization test in chloride-thiosulfate (NH_4Cl + $Na_2S_2O_3$) solution revealed lower corrosion current (I_{corr}) (0.42 ± 0.02 μA/cm^2 and 0.086 ± 0.001 μA/cm^2 Vs. 0.76 ± 0.05 μA/cm^2), lower passivation current (I_{pass}) (1.45 ± 0.03 μA/cm^2 and 1.83 ± 0.07 μA/cm^2 Vs. 1.98 ± 0.04 μA/cm^2), and approximately six-fold higher breakdown potential (E_{bd}) for Fe- and Al-based coatings than those of wrought 316L stainless steel. Electrochemical Impedance Spectroscopy (EIS) of both films showed 4- and 2-fold higher charge transfer resistance (R_{ct}), 7- and 2.5-times higher film resistance (R_f), lower film capacitance values (Q_f) (10 ± 2.4 μS-s^{a}cm^{-2}, and 5.41 ± 0.8 μS-s^{a}cm^{-2} Vs. 18 ± 2.21 μS-s^{a}cm^{-2}), and lower double-layer capacitance values (Q_{dl}) (31.33 ± 4.74 μS-s^{a}cm^{-2}, and 15.3 ± 0.48 μS-s^{a}cm^{-2} Vs. 43 ± 4.23 μS-s^{a}cm^{-2}), indicating higher corrosion resistance of the thin films. Cyclic Voltammetry (CV) scan exhibited that the passive films formed on the Fe- and Al-based coatings were more stable and less prone to pitting corrosion than the wrought 316L stainless steel. The surface morphology of both films via SEM endorsed the CV scan results, showing better resistance to pitting corrosion. Furthermore, the thermal analysis via TGA and DSC revealed the excellent thermal stability of the thin films over a wide temperature range typically observed in oil-gas industries.

1. Introduction

Carbon steel, low alloy steel, Cr-Mo steel, stainless steel, and nickel-based alloys are broadly used in oil-gas industries due to their good mechanical strength, corrosion resistance, and low cost [1]. However, the equipment used in these industries are exposed to high temperature, high pressure, and corrosion, that lead to rapid material degradation. Different corrosive elements resulting from the production and processing of oil and gas lead to sudden failure of machine components due to pitting corrosion. For example, Ni-based alloys suffer pitting and crevice corrosion in oxidizing halide-containing environments [2]. Similarly, 316L stainless steel undergoes localized corrosion in aggressive environments due to the unstable passive film formed on the surface [3].

The corrosive species found in the oil-gas exploration fields are H_2S, CO_2, SO_2, amines, cyanides, salts, naphthenic acids [4,5]. H_2S is the most destructive among those species, leading to pitting, crevice, fatigue, and stress corrosion cracking of steel in the oil and gas purification process [6]. In the presence of H_2S and other sulfur elements in crude oil, FeS film is formed on different stainless steel components, such as valve equipment, pipelines, oil storage tank etc. [6]. The reaction of FeS with water and oxygen produces polythionates and other oxyanions, such as thiosulphate ($S_2O_3^{2-}$) [7]. Furthermore, $S_2O_3^{2-}$ can produce elemental sulfur, which can further reduce to H_2S via chemical reaction. Due to flammability and noxiousness of H_2S, $S_2O_3^{2-}$ is used as a replacement of toxic H_2S to conduct corrosion studies in aggressive oil and gas environment [8]. Nevertheless, $S_2O_3^{2-}$ itself is not sufficient enough to corrode the steel surface, as it is unable to break the passive film [9,10]. Chloride ion (Cl^-), especially in the form of NH_4Cl, has also been reported as one of the potentially harmful corrosive elements for equipment and piping in oil refinery industries [11,12]. Hence, a number of studies have been

* Corresponding author.
E-mail address: shabi1i@cmich.edu (I. Shabib).

https://doi.org/10.1016/j.pnsc.2021.09.005
Received 23 April 2021; Received in revised form 1 September 2021; Accepted 8 September 2021

conducted to delve into the combined effect of $S_2O_3^{2-}$ and Cl^- ions on electrochemical behavior of stainless steel [3,10,11].

Surface modification through coating is a commonly employed technique to prevent corrosion in aggressive environment typically observed in oil and gas industry. Magnetron sputtering, a physical vapor deposition (PVD) technique, is one of the ways to produce high-quality coating over a base material. Transition metal nitride (TMN) coatings such as TiN, CrN, TiAlN, and NbN, fabricated by magnetron sputtering, have been broadly used to improve corrosion resistance, thermal and chemical stability [13], wear-resistance, and higher hardness [14], making TMNs suitable for coating applications to protect base materials in corrosive environment. Several studies have found that the addition of aluminum (Al) to binary metal film increases the electrochemical corrosion resistance [15,16]. Enhancement of corrosion resistance by adding Al is attributed to the formation of Al_2O_3 passive film on the surface, which prevents the degradation of the material during chemical attack [17]. Besides, Oxide coatings, such as TiO_2, Al_2O_3, ZrO_2, on stainless steel, have been found to exhibit higher corrosion-resistant in aggressive environments than uncoated substrate [18,19]. Zavareh et al. [20] have studied the corrosion behavior of Al_2O_3-TiO_2 coating applied on carbon steel. The coating has shown good corrosion resistance in crude oil and 3.5% Sodium Chloride (NaCl) compared to the bare substrate. Other studies suggest that Fe-based metallic glasses coatings such as, Fe-Cr-Mo-C-B, Fe-Ni-Mo-Cr-P-C-B etc., demonstrate higher corrosion resistance as well as good mechanical strength [21,22].

In this research, $Fe_{44}Al_{34}Ti_7N_{15}$ and $Al_{61}Ti_{11}N_{28}$ thin-film metallic glasses (TFMGs) have been fabricated to protect the base materials from deterioration and compare their microstructural features and electrochemical performance with wrought 316L SS in Cl^- and $S_2O_3^{2-}$ solution simulating the corrosive atmosphere of oil and gas industries. Sputtered thin films are characterized by X-ray diffraction (XRD), energy-dispersive X-ray spectroscopy (EDS), and X-ray photoelectron spectroscopy (XPS) techniques. Electrochemical measurements, such as potentiodynamic polarization, electrochemical impedance spectroscopy (EIS), and cyclic voltammetry (CV), are conducted to analyze the corrosion behavior of the thin films in Cl^- and $S_2O_3^{2-}$ solution. Post corrosion surface analysis via Scanning Electron Microscopy (SEM) is also carried out to support the research findings. Furthermore, thermal analyses of both thin films are performed via Thermogravimetry Analysis (TGA) and Differential Scanning calorimetry (DSC).

2. Experimental

2.1. Fabrication of the thin films

A Magnetron co-sputtering system, Nano 36^{TM} by Kurt J. Lesker Company®, was used to deposit Fe- and Al-based thin films on silicon wafer substrate using FeAl (60-40 at. %), Al, and TiN targets. The substrate was not heated during the film deposition process. Before starting the film deposition, the sputtering chamber was evacuated to a vacuum pressure of $4\sim7 \times 10^{-6}$ Torr. Highly purified argon gas was delivered to the chamber, and a working pressure of 1.3×10^{-2} Torr was maintained during the film deposition. For the Fe-based film, the FeAl target was sputtered via a DC source powered at 200 W and TiN was sputtered simultaneously via a RF source powered at 140 W. For the Al-based film, the Al and TiN targets were co-sputtered via the DC and RF sources powered at 100 W and 120 W, respectively. The deposition time for both the films was set to 60 min.

2.2. Microstructure and compositional analysis

The grazing incidence X-ray diffraction (XRD) was carried out over a 2θ range between 15^0 and 85^0 with a grazing angle 1^0 and a step size of 0.1^0 to analyze the structural phase of the films. The XRD pattern for wrought 316L SS was obtained using Rigaku Ultima IV Diffractometer equipped with Cu Kα radiation source ($\lambda = 1.54$ A^o) at a speed of 1°/min (step size 0.02°) to analyze the structural differences with the fabricated films. The surface chemistry of the fabricated thin films was studied by X-ray photoelectron spectroscopy (XPS). The X-Ray Photoelectron Spectrometer (Thermo Fisher Scientific K-Alpha) provided with Al Kα source was used to obtain survey spectra from 0 to 1000 eV at an energy resolution of 1eV (at 100 eV pass energy). The spot size was 400 μm, and pressure inside the chamber was maintained below 5×10^{-7} mbar. The binding energy scale was calibrated by standardizing C 1s at 284.8 eV. The high-resolution spectra were obtained with an energy resolution of 0.05 eV (at 50 eV pass energy) and deconvoluted using Gaussian-Lorentzian-Cross function after adopting Shirley method for background subtraction. Hitachi S-3400-II Scanning Electron Microscope (SEM) was employed to perform the microstructure analysis of both the fabricated films and wrought 316L SS after potentiodynamic polarization test. Thermogravimetric analysis (TA Instruments, TGA 25) was conducted to investigate the thermal stability of the fabricated films. The TGA curves of TFMGs and Si wafer were obtained at a heating rate 20 °C/min from 100 °C to 1000 °C in a ceramic crucible for three repeatable cycles. Differential scanning calorimeter (TA Instruments, DSC 25**)** was employed to observe the heat flow and material transition characteristics by heating the samples in a graphite crucible from 100 °C to 700 °C with a heating rate of 20 °C/min. The TGA and DSC measurements were performed in an inert environment by supplying nitrogen (N_2) gas. The energy dispersive X-ray spectrometry (EDS) analyzer coupled with SEM system was used to determine the fabricated film's chemical compositions.

2.3. Electrochemical measurement

Electrochemical characterizations of the sputtered thin films over silicon wafers and bare wrought 316L SS samples were performed in 1 M NH_4Cl+1 M $Na_2S_2O_3$ solution simulating oil and gas environment. High purity Milli-Q water and analytical grade chemicals were used to prepare NH_4Cl and $Na_2S_2O_3$ solutions. The pH of 1 M NH_4Cl, 1 M $Na_2S_2O_3$, and 1 M NH_4Cl+1 M $Na_2S_2O_3$ solutions were 5.25, 6.77, and 6.37, respectively. The experiments were performed in a three-electrode Gamry Reference 1000E potentiostat. A saturated calomel electrode (SCE) and a platinum coil were used as the reference and counter electrode, respectively. The thin films and wrought 316L SS samples were used as the working electrode.

Before starting the electrochemical measurements, the working electrode was kept in prepared solution for 4 h to achieve a potential stability of 0.01 mV/s by measuring open circuit potential (OCP). The potentiodynamic polarization (PD) test was conducted with a scan rate of 1 mV/s from –0.5 V to + 2 V (vs. OCP) for Fe and Al-based thin films. The PD scan of the wrought 316L SS sample was carried out with the same scan rate from –0.5 V to +0.6 V (vs. OCP). The corrosion current density and corrosion potential were extracted via a standard technique, i.e., the application of Tafel extrapolation by linear fitting of the polarized zones within ±50 mV of OCP [23]. Electrochemical impedance spectroscopy (EIS) was done with A.C. amplitude of ±5 mV_{rms} (DC voltage was 0 at open circuit potential) in the frequency range of 100 kHz to 0.01 Hz, recording 10 data points per decade. Three consecutive cyclic voltammetry (CV) cycles were recorded at a scan rate of 50 mV/s started from –1.2 V to + 0.8 V (vs. SCE) in the anodic direction and then reversing the scanning path to direction of the initial point (–1.2 V vs. SCE) for all test samples. Each electrochemical experiment was repeated at least three times to ensure reproducibility and consistency.

3. Results and discussion

3.1. Microstructure and composition analysis

The compositions of the thin films in atom percentage obtained via EDS are shown in Table 1. Henceforth, the quaternary $Fe_{44}Al_{34}Ti_7N_{15}$

Table 1
Composition analysis (atomic percentage) of the metallic glasses.

Systems	Fe	Al	Ti	N
FATN	44	34	7	15
ATN		61	11	28

Table 2
Atomic radius mismatch (%) and heat of mixing (kJ/mol) of the atomic pairs.

Film	FATN and ATN system					
Atomic pair	Fe-Al	Fe-Ti	Fe-N	Al-Ti	Al-N	Ti-N
Atomic mismatch (%)	15.34	17.74	65.5	2.08	90.89	94.86
Heat of mixing (kJ/mol)	–11	–17	-87	–30	–92	–190

and ternary $Al_{61}Ti_{11}N_{28}$ thin films will be referred to as FATN and ATN, respectively. The composition (in wt.%) of the wrought 316L stainless steel was 18Cr-12Ni-2.3Mn-2.1Mo-0.06P-0.04O-0.03C-0.03S-Fe Balance, supplied by the manufacturer.

The XRD results of FATN, ATN, and 316L SS are presented in Fig. 1. The XRD pattern of 316L SS displays very distinct sharp peaks correspond to $\gamma(111)$, $\gamma(200)$, and $\gamma(220)$ crystallographic planes at 2θ location of 43.65°, 50.81°, and 74.72°, respectively. In contrast, FATN thin film exhibits a broad peak at 2θ value of ~40° to ~ 46°, and ATN thin film shows the peak at~ 35° to ~ 45°, which indicate the amorphous microstructure of both films. According to Greer [24], the formation of metallic glass occurs due to the confusion of involved elements to gain a viable crystal structure. Furthermore, according to the empirical rules suggested by Inoue [25], the multicomponent systems having three or more elements, atomic size mismatch of more than 12%, and negative heat of mixing result in an amorphous structure.

The FATN and ATN metallic glass systems fabricated via magnetron sputtering complied well with the empirical rules of Inoue, as both the films consist of 3 or more elements, exhibiting more than 12% atomic mismatch between atom pairs except Al-Ti (2.08%), and having negative heat of mixing for all the atomic pairs as listed in Table 2. Hence, it can be deduced that both the TFMGs possess amorphous structure, which is also supported by GI-XRD results.

The XPS survey of FATN and ATN films are shown in Fig. 2(a) and Fig. 2(g), respectively. The high-resolution de-convoluted spectra of all the constituent elements of FATN and ATN thin films are shown in Fig. 2(b–f) and Fig. 2(h–k), respectively. The survey spectrum in Fig. 2(a) shows pronounced peaks of Fe 2p, Al 2p, Ti 2p, N 1s, O 1s, and C 1s, whereas the survey spectrum in Fig. 2(g) shows the peaks of Al 2p, Ti 2p, N 1s, O 1s, and C 1s. C 1s peak is observed in both XPS surveys, which may be a result of carbon contamination from atmosphere as well as XPS instruments. The deconvoluted Fe 2p spectra of FATN thin film consists of Fe $2p_{1/2}$, Fe $2p_{3/2}$, satellite, and metallic peaks. The Fe $2p_{3/2}$ peaks (Full width at half maximum, FWHM = 3.78 eV) at 710.48 eV and 711.73 eV indicate the presence of Fe^{2+} and Fe^{3+}on the surface, respectively [26]. Moreover, a satellite peak of Fe $2p_{3/2}$ (FWHM = 1.57 eV) was observed at 719.48 eV, approximately 8.6 eV higher binding energy than the Fe $2p_{3/2}$ peak, which proves the presence of Fe^{3+} species on the surface [27]. The metallic Fe also appeared on the surface, which corresponds to the binding energy of 707.28 eV of the Fe 2p spectrum [28]. All those prominent peaks prove the presence of iron oxide in the form of Fe_3O_4, FeO, and Fe_2O_3 with some amount of metallic Fe on the surface of the FATN sample [29]. Ti 2p spectra (as shown in Fig. 2 (d & i)) consist of pronounced doublets of Ti $2p_{3/2}$ and Ti $2p_{1/2}$.

The binding energy of 458.23–459.65 eV for Ti $2p_{3/2}$ (FWHM = 1.78 eV, and 2.17 eV for FATN and ATN, respectively) is in agreement with the literature [30], which indicates Ti^{4+} for both films. Ti^{3+} was observed for both films at binding energy intervals of 459.13–461.1 eV [30]. Additionally, the Ti 2p spectrum of FATN and ATN films shows a peak approximately at 454.6–455.1 eV (FWHM = 1.81 eV, and 2.92 eV for FATN and ATN, respectively), which can be attributed to the Ti-N bond [31]. Al 2p spectra (as shown in Fig. 2 (c & h)) showing peaks approximately at 74–75 eV (FWHM = 1.63 eV, and 1.45 eV for FATN and ATN, respectively), which correspond to Al^{3+} species on the surface of both films, while metallic Al peak is observed at 72.8 eV (FWHM = 1.48eV) for ATN thin film [28]. As Al content is almost double in ATN film than FATN, metallic Al is observed only in ATN film. In Fig. 2 (e), the peaks at around 396.6 eV (FWHM = 1.51 eV) and 399.3 eV (FWHM = 3.07 eV) binding energies are associated with Ti-N and Ti-O-N bond, respectively, for FATN thin film [31]. The N 1s spectra shows a broad peak (Fig. 2(j)) at 396.8 eV (FWHM = 4.16 eV), indicating the presence of TiN on the ATN thin film surface, which is also validated by the deconvoluted Ti 2p spectrum of that film (Fig. 2(i)). The O 1s spectrum is composed of two overlapping peaks referred to O^{2-} (metal oxide) and OH^- (non-lattice oxygen) [32]. O^{2-} peak is more intense than the OH^-, as shown in the deconvoluted O 1s spectrum in Fig. 2 (f and k), which proves the metallic oxide film formation on the surface of both TFMGs.

3.2. Electrochemical analysis

3.2.1. Potentiodynamic polarization

Potentiodynamic polarization plots of FATN, ATN, and wrought 316L SS are shown in Fig. 3(a). The electrochemical properties, such as corrosion potential (E_{corr}), corrosion current density (I_{corr}), passivation current density (I_{pass}), and breakdown potential (E_{bd}), extracted from potentiodynamic polarization curves are shown in Table 3. The E_{corr} value of wrought 316L SS (-126 ± 8.7 mV_{SCE}) was relatively higher than FATN (-386 ± 9 mV_{SCE}) and ATN (-816 ± 7 mV_{SCE}) thin films. The higher negative shift of corrosion potentials of thin films represents the presence of relatively active species on the sputtered samples than wrought 316L

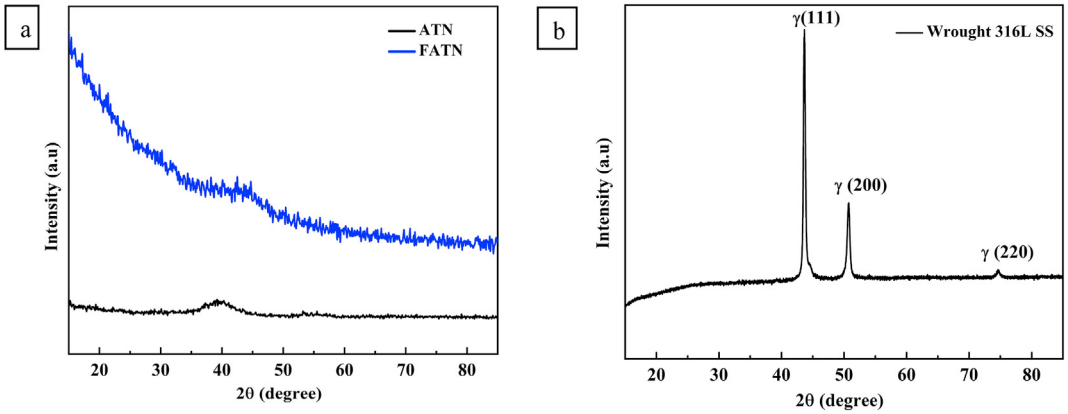

Fig. 1. (a) GI-XRD pattern of FATN and ATN metallic glasses, and (b) XRD of wrought 316L SS.

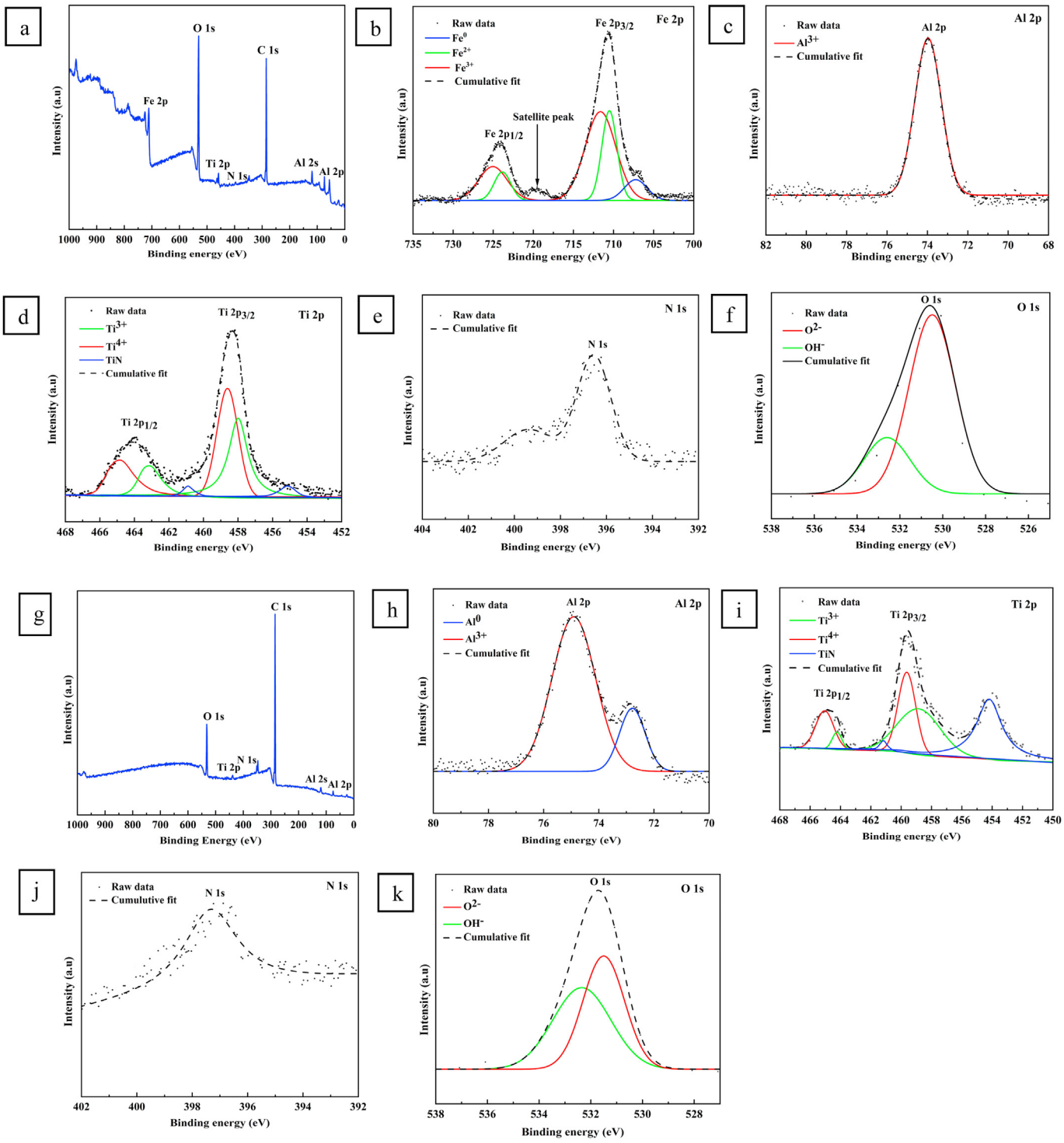

Fig. 2. XPS Survey spectra of (a) FATN, and (g) ATN. High resolution deconvoluted spectra of constituent elements of (b–f) FATN, and (h–k) ATN.

SS. The dissolution process of these active species, i.e., the inherent oxide films, was found to be more intense for ATN than those of FATN and wrought 316L SS (during the cathodic scan). However, ATN exhibited approximately one order of magnitude lower I_{corr} value (0.086 ± 0.001 μA/cm^2), than the wrought 316L SS (0.76 ± 0.05 μA/cm^2). The FATN thin film also showed lower current density (0.42 ± 0.02 μA/cm^2) than the wrought 316L SS. The lower I_{corr} values of both the films demonstrate higher corrosion resistance than wrought 316L SS in Cl^- and $S_2O_3^{2-}$ solution. During anodic potentiodynamic polarization scan, ATN and FATN displayed relatively lower anodic current density, referred to as passivation current density (I_{pass}) (1.83 ± 0.07 μA/cm^2 and 1.45 ± 0.03 μA/cm^2, respectively) compared to wrought 316L S.S. (1.98 ± 0.04 μA/cm^2). Additionally, a larger anodic passive region was observed for both TFMGs, while no such passive region was observed for wrought 316L SS (Fig. 3(a)). The larger anodic passive region with lower passivation current values indicates that denser and more protective passive layer is formed on TFMGs than the wrought 316L SS [33,34]. At higher anodic potential during polarization, a rapid increase in current density represents passive film breakdown with a small change in potential (referred to breakdown potential, E_{bd}).

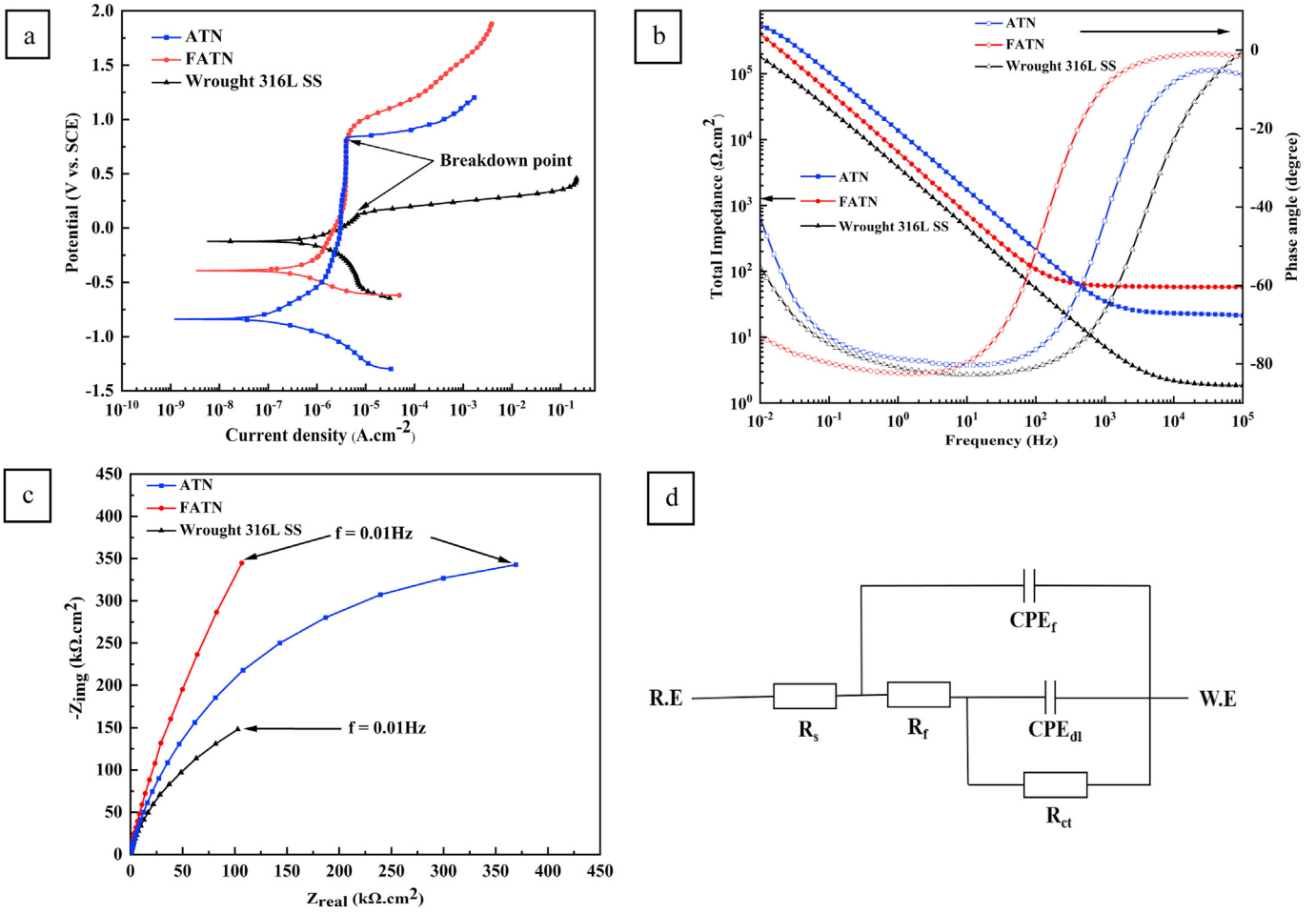

Fig. 3. Electrochemical responses of ATN, FATN, and wrought 316L SS in Cl^- - $S_2O_3^{2-}$ environment. (a) Potentiodynamic polarization plots, (b) Bode plots, (c) Nyquist plots, and (d) Equivalent Electrical Circuit (EEC) model of the systems.

Table 3
Quantitative information of electrochemical parameters extracted from Potentiodynamic polarization scans (n = 3).

Systems	E_{corr} (mV)	I_{corr} (μA/cm^2)	E_{bd} (mV)	I_{pass} (μA/cm^2)	E_{bd} -E_{corr} (mV)
ATN	-816 ± 7	0.086 ± 0.001	852 ± 21	1.83 ± 0.07	1672 ± 38
FATN	-386 ± 9	0.42 ± 0.02	858 ± 19	1.45 ± 0.03	1240 ± 38
Wrought 316L SS	-126 ± 8.7	0.76 ± 0.05	132 ± 6	1.98 ± 0.04	258 ± 5

Both ATN and FATN TFMGs demonstrated more than 6 times higher breakdown potential (852 ± 21 mV and 858 ± 19 mV, respectively) compared to the wrought 316L SS (132±6 mV), which implies that the passive films formed on the TFMGs are more pitting corrosion resistance than wrought 316L SS. The width of the passivation region (E_{bd}-E_{corr}) is often used to quantify the resistance of the samples against pitting corrosion [35]. The pitting resistance (E_{bd}-E_{corr}) values of ATN (1672 ± 38 mV) and FATN (1240 ± 38 mV) were more than 6 and 4 times higher than wrought 316L SS (258 ± 5 mV), respectively, which indicate superior stability of the passive oxide film. Thus, it can be inferred from the potentiodynamic polarization that both TFMGs demonstrate improved corrosion resistance compared to wrought 316L SS in Cl^- and $S_2O_3^{2-}$ solution.

Magnetron sputtered AlTiO thin film on 316L SS, studied by Tian et al. [36], exhibited two orders of magnitude lower corrosion current density than substrate material in 3.5 wt% NaCl solution. Multilayered Ti/TiN/TiSiN coating on 304 stainless steel showed more positive corrosion potential, almost half of corrosion current density, and a wider passive region than substrate materials in 3.5 wt% NaCl aqueous solution [37]. Li et al. developed Fe-based ($Fe_{48}Mo_{14}Cr_{15}Y_2C_{15}B_6$) TFMGs which exhibited higher pitting potential (E_{pit} = 900 mV V SCE), wider passivation region, and lower passivation current density (0.1–1 μA/cm^2) compared to 304 SS alloy [38]. Obeydavi et al. studied electrochemical characteristics of magnetron sputtered $Fe_{44}Cr_{15}Mo_{14}Co_7C_{10}B_5Si_5$ thin-film metallic glass in 5 wt% NaCl solution and found four times lower corrosion current density, approximately two times lower passivation current, and higher pitting potential (E_{pit} = 481.1 mV V SCE) compared to 304 SS [39]. Although the fabricated ATN and FATN TFMGs are compositionally different than those reported in the previous studies, the obtained electrochemical responses are qualitatively similar.

The structural and compositional homogeneity are two major factors contributing to the superior corrosion resistance of TFMGs [40]. However, Wang et al. reported that passive films formed on the amorphous alloys are more compact and less defective, indicating higher corrosion resistance than the single crystal counterpart [23]. The passivation of the surface can be further enhanced by the "atomic mobility" of the structure [41]. According to the study conducted by Tang et al. metallic glasses are thermodynamically metastable and have higher energy, resulting in

higher atomic mobility. Thus, the atoms in metallic glasses are electro-chemically more active than the crystalline system [41], leading to relatively faster passivation. Therefore, the barrier type oxide layer formation on FATN and ATN thin films at very low I_{pass}, and the higher stability of the passive layer at high anodic potentials may offer an explanation of enhanced corrosion resistance of the amorphous structure. Furthermore, the chemical composition is another well-known factor influencing corrosion behavior. Hence, the observed corrosion properties of FATN and ATN thin films are attributed to the major film species, such as Fe, Al, Ti. Oxidation of these species leads to quick surface enrichment of their corresponding oxides, as validated by XPS (Fig. 2).

In contrast, the increased corrosion rate of wrought 316L SS as depicted by higher corrosion current density in Cl^- and $S_2O_3^{2-}$ solution occurs due to the generation of the corrosive element-sulfur [42]. The element sulfur can form FeS film by reacting with Fe^{2+} within the pH 4 to 8, accelerating the corrosion rate of 316L SS [12,43]. The wrought 316L SS showed lower breakdown potential, as shown in Fig. 3(a), indicating that the stainless steel is susceptible to pitting corrosion due to Cl^- attack. The breakdown mechanism of the passive film with the presence of Cl^- was investigated by Burstein et al. [44]. According to this study, Cl^- may be adsorbed on the surface and penetrate the oxide film leading to the soluble metal chloride formation. The passive oxide film may be ruptured when the concentration of metallic chlorides in the oxide film is relatively higher compared to metal oxide, and consequently the stable pits form. Some other studies have also been conducted illustrating the penetration of Cl^- in the oxide film, causing passive film breakdown [45,46]. On the contrary, the denser passive oxide films formed on the TFMGs offer higher protection against corrosive elemental sulfur and are less vulnerable to pit initiating Cl^- attack.

3.2.2. Electrochemical impedance spectroscopy

The bode and Nyquist plots obtained from the Electrochemical Impedance Spectroscopy (EIS) test are shown in Fig. 3(b) and (c), respectively. To extract the quantitative electrochemical parameters from EIS, an equivalent electrical circuit (EEC) model shown in Fig. 3(d) was employed to fit the experimental EIS spectra. The EEC elements comprise of a solution resistance (R_s), charge transfer resistance (R_{ct}), film resistance (R_f), constant phase element for the electric double layer (CPE_{dl}), and constant phase element across the passive film (CPE_f). At high frequency region (~100 KHz), the phase angles of the bode plot were approaching zero, which indicates that the impedance is characterized by the resistance called solution resistance (R_s). The negative phase angle of -80° was observed in the frequency range of approximately 10 Hz–1 Hz, representing the capacitive behavior of the electric double layer and/or passive oxide film. Due to the non-uniform distribution of charges across the double layer and surface roughness, ideal capacitive behavior was not observed [47] (i.e., phase angle shift is greater than –90° as opposed to pure capacitive response of phase angle –90°). Therefore, the capacitive behavior within that frequency range is illustrated by constant phase elements CPE_{dl} and CPE_f, and their impedance can be defined as,

$$Z_{CPE} = [Q(j\omega)^a]^{-1}$$

where $j = \sqrt{-1}$ refers to the imaginary part of the impedance, ω is the angular frequency, Q is the imaginary admittance, and a is the exponent of CPE of value $0 < a < 1$. The parallel combination of R_{ct} and CPE_{dl} represents the faradaic and non-faradaic processes at the electrode/electrolyte interface. From the bode plot shown in Fig. 3(b), considerably higher impedance values at the low-frequency region (at $f = 0.01$ Hz) of ATN and FATN systems (503.9 KΩ-cm^2, and 360.9 KΩ-cm^2 respectively) compared to wrought 316L SS (180.3 KΩ-cm^2) demonstrate improved barrier characteristics of the oxide layer formed on the thin-film surface.

The Nyquist plot shown in Fig. 3(c) was comprised of depressed semicircles, and the intersection of the extrapolated semicircle with the Z_{real} axis at the low-frequency region represents the R_t of the system, including R_s, R_{ct}, and R_f. Thus, the large diameter of the depressed semicircles indicates better corrosion resistance. From the Nyquist plot, the diameter of the three systems can be ranked in the order of FATN > ATN > wrought 316L SS, which illustrates better corrosion resistance of the TFMGs.

The quantitative information of each element in the electrical equivalent circuit model obtained by fitting EIS spectra is shown in Table 4. The goodness of fit, assessed by the chi-squares (χ2) values, was maintained in the order of 10^{-3}. Both ATN and FATN thin film metallic glasses showed 2–5 fold higher R_{ct} values (374.7 ± 10.8 KΩ-cm^2, and 702.66 ± 10 KΩ-cm^2, respectively) and approximately 2.5–7 times higher R_f values (490.7 ± 9.7 KΩ-cm^2, and 1350 ± 18.4 KΩ-cm^2, respectively) compared to wrought 316L SS ($R_{ct,wrought} = 157 \pm 7.5$ KΩ-cm^2, and $R_{f,wrought} = 184.6 \pm 8.9$). Additionally, R_t values of ATN and FATN (864 ± 13.85 KΩ-cm^2 and 2053 ± 27.26 KΩ-cm^2) were approximately 2.5 and 6 times higher than wrought 316L SS (342 ± 12.47 KΩ-cm^2), respectively, which revealed superior corrosion resistance of TFMGs. Relatively lower Q_f values associated with the passive film of ATN (5.41 ± 0.8 μS-s^{a}cm^{-2}) and FATN (10 ± 2.4 μS-s^{a}cm^{-2}) indicate better barrier characteristics than wrought 316L SS (18 ± 2.21 μS-s^{a}cm^{-2}). Moreover, the Q_{dl} values of ATN (15.3 ± 0.48 μS-s^{a}cm^{-2}) and FATN (31.33 ± 4.74 μS-s^{a}cm^{-2}) were smaller than wrought 316L SS (43 ± 4.23 μS-s^{a}cm^{-2}), indicating less defective structure of oxide films of TFMGs. The smaller impedance (R_{ct} and R_f) and larger capacitance values (Q_{dl} and Q_f) indicate higher charge transport at the working electrode-electrolyte interface, resulting in higher Cl^- inclusion within the defective passive film. Also, the presence of $S_2O_3^{2-}$ in the solution increases the number of defective sites in the passive film [48], facilitating the Cl^- attack into the oxide film and increasing the probability of passive oxide film breakdown. In contrast, the higher impedance and lower capacitance at the TFMGs-electrolyte interface suggest a more stable and protective passive oxide film formed at the ATN and FATN surface in Cl^- and $S_2O_3^{2-}$ solution.

3.2.3. Cyclic voltammetry

Three consecutive cyclic voltammograms for each sample are presented in Fig. 4. Three anodic peaks were observed (A_1, A_2, and A_3) for ATN film, as shown in Fig. 4(a). A_1 peak at around -300mV may correspond to the oxidation of Al to Al^{3+}. With the increase of applied potential, current density increased, showing a peak A_2, which may correspond to the formation of $Al(OH)_3$ or aluminum chloride ($AlCl_3$) species [49]. A_3 peak was also observed at approximately 350 mV, representing the formation of TiO_2 due to the oxidation of Ti according to the following equation (1) [50].

$$Ti + 2H_2O \leftrightarrow TiO_2 + 4H^+ + 4e^- \quad (1)$$

There were no anodic peaks observed on subsequent CV scans (2nd and 3rd cycle), demonstrating surface passivation of the ATN film. Furthermore, no cathodic peaks were observed, indicating the formation of stable passive film on the surface. Three anodic peaks were observed for FATN and wrought 316L SS samples shown in Fig. 4(b) and (c), respectively. The gradual increase of current density before the peak A_1 indicates the formation of $Fe(OH)_2$ according to equation (2) [51].

$$Fe + 2H_2O \leftrightarrow Fe(OH)_2 + 2H^+ + 2e^- \quad (2)$$

A_1 peaks, observed at approximately ~ -830mV$_{SCE}$, represent the formation of Fe_3O_4 due to the oxidation of Fe and $Fe(OH)_2$ [51]. Passivation of the surface was continued with the increase of potential, and another peak A_2 appeared at ~ -160mV$_{SCE}$ and at ~ -200mV$_{SCE}$ for FATN and wrought 316L SS samples, respectively. These peaks correspond to the formation of $Fe(OH)_3$ species via the following equation (3) [52].

$$Fe(OH)_2 + H_2O \leftrightarrow Fe(OH)_3 + H^+ + e^- \quad (3)$$

Current density decreased after A_2, illustrating the passive film

Table 4
Quantitative data obtained by fitting the Equivalent Electrical Circuit (EEC) model to the experimental EIS spectra (n = 3).

Systems	R_s (Ω.cm^2)	R_f (KΩ.cm^2)	Q_f (μS-s^{a}cm^{-2})	R_{ct} (KΩ.cm^2)	Q_{dl} (μS-s^{a}cm^{-2})	R_t (KΩ.cm^2)	Goodness of fit (10^{-3})
ATN	19.12 ± 3.7	490.7 ± 9.7	5.41 ± 0.8	374.7 ± 10.8	15.3 ± 0.48	864 ± 13.85	0.86 ± 0.09
FATN	42.35 ± 2.1	1350 ± 18.4	10 ± 2.4	702.66 ± 10	31.33 ± 4.74	2053 ± 27.26	0.42 ± 0.29
Wrought 316L SS	4.05 ± 2.5	184.6 ± 8.9	18 ± 2.21	157 ± 7.5	43 ± 4.23	342 ± 12.47	0.45 ± 0.07

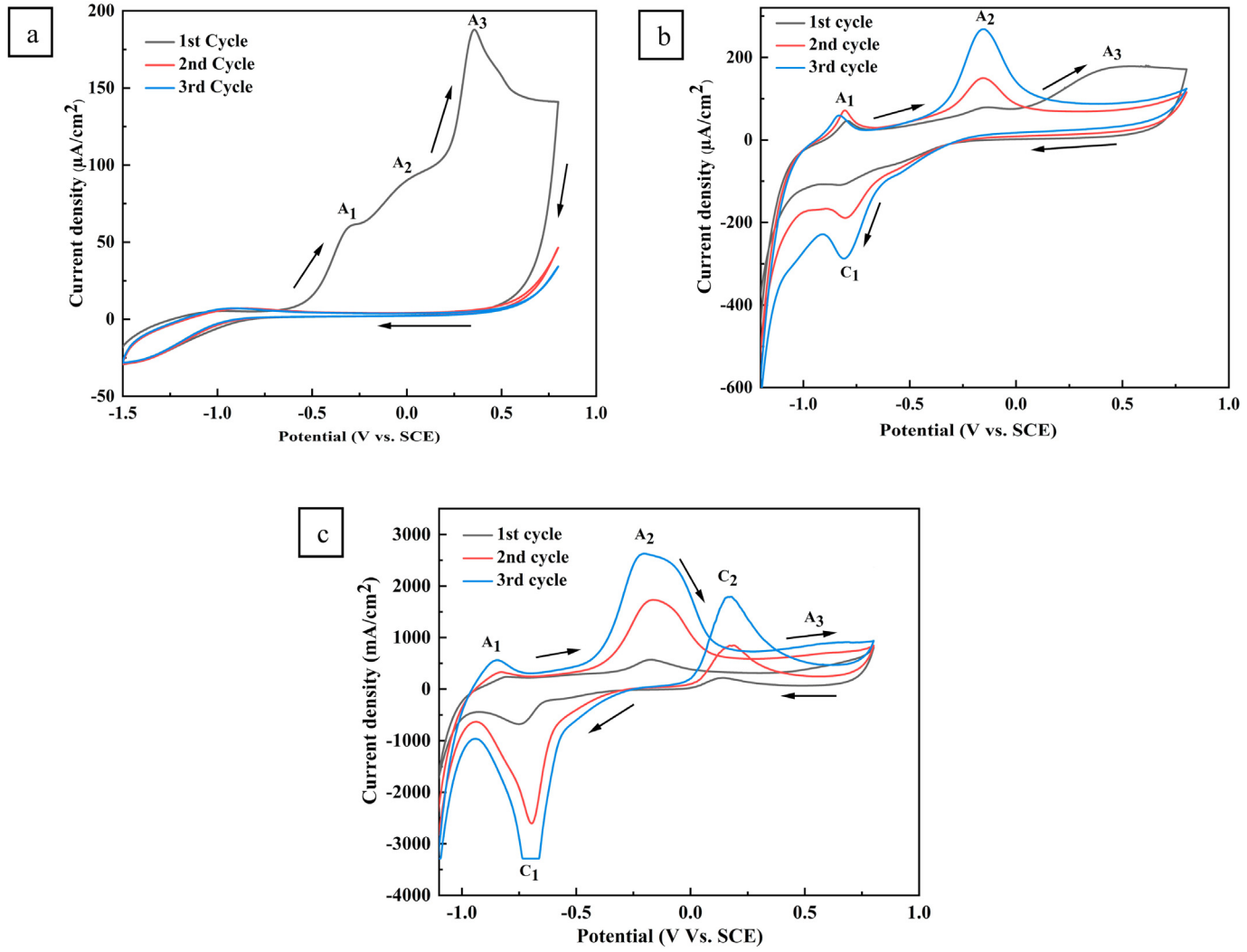

Fig. 4. Cyclic voltammograms (CV) of the samples in 1 M NH_4Cl+1 M $Na_2S_2O_3$ solution. (a) ATN, (b) FATN, and (c) Wrought 316L SS.

formation on the surface. In the subsequent scans, the passive current density of wrought 316L SS beyond the A_2 peak was much higher than FATN, which corresponds to the Cl^- incorporation into the passive layer of wrought 316L SS according to the following equation (4) [52].

$$Fe(OH)_3 + Cl^- \leftrightarrow Fe(OH)Cl^+ + 2OH^- \quad (4)$$

In the 2nd and 3rd cycles, A_2 peaks appeared over a wide range of potential for wrought 316L SS, which correspond to the sulfur adsorption into the passive layer via equation (5) and/or equation (6) [53]

$$S_2O_3^{2-} + H^+ \leftrightarrow S + HSO_3^- \quad (5)$$

$$S_2O_3^{2-} + 6H^+ + 4\,e^- \leftrightarrow 2S + 3H_2O \quad (6)$$

The A_3 peak appeared at ~450 mV for FATN thin film may represent the oxidation of Al to Al^{3+} resulting in $Al(OH)_3$ formation, whereas A_3 peak appeared at ~690 mV for wrought 316L SS denotes the production of CrO_4^{2-} due to the oxidation of inherent Cr_3O_4 via following equation (7) [51].

$$Cr_2O_3 + 5H_2O \leftrightarrow 2CrO_4^{2-} + 10H^+ + 6e^- \quad (7)$$

During the cathodic scan of the CV test, one cathodic peak was observed for FATN samples while two cathodic peaks were observed for wrought 316L SS. The cathodic peak C_1 for both FATN and wrought 316L SS samples corresponds to the counter peak of anodic peak A_1. It is evident from the CV scan of wrought 316L SS that the intensity of the C_1 peak was much intense than the A_1 peak, which indicates the complete reduction of Fe^{2+}. The C_2 peak for the wrought sample appeared at ~160 mV, indicating the additional Sulfur adsorption into the passive film. Moreover, a positive hysteresis loop was observed for wrought samples indicating passive film breakdown, which facilitates the pitting

corrosion on the surface [54]. Overall, the passive film formed on ATN and FATN samples showed better stability over a wide potential range, while wrought 316L SS was susceptible to pitting corrosion due to passive film breakdown.

3.2.4. Post corrosion surface analysis

The SEM images of ATN, FATN, and wrought 316L SS samples are presented in Fig. 5. The surface morphology of ATN thin film showed granular corrosion product on the surface (Fig. 5(a)), and FATN showed a more refined appearance with less number of corrosion pits (Fig. 5(c)). No film delamination was observed for both ATN and FATN samples. Upon magnification of the SEM images up to 50 μm, it was observed that the corrosion products were almost uniformly distributed over the surface of ATN thin film (Fig. 5(b)); however, no pits were observed on the surface. A relatively less amount of corrosion products was formed on FATN, which were randomly scattered over the surface (Fig. 5(d)).

These corrosion products may be comprised of oxides and chlorides of Fe and Al [55]. Sulfur may also be present in the corrosion products as reported by other researchers [54]. In addition, some tiny black particles, which were micron-ranged pits in the range of ~2–3 μm, were observed on FATN samples (Fig. 5(d)). On the contrary, the surface morphology of wrought 316L SS showed a multitude of pits of sizes in the range of 20–90 μm (Fig. 5(e)). The magnified image of the corroded wrought 316L SS showed a comparatively more broad and deeper pit of size ~90 μm (Fig. 5(f)), which is 40–50 times higher than those observed in TFMGs. From the SEM images, it is evident that the wrought 316L SS was more susceptible to localized corrosion than the thin film samples.

3.3. Thermal analysis

TGA curves show the percentage of weight change with respect to temperature. The fabricated thin films (ATN and FATN) and Si wafer showed no mass loss in three repetitive cycles (Fig. 6(a–c)), indicating thermal stability of the samples over a wide temperature range from 100 °C to 1000 °C. A slight increase in weight was observed for all the samples which may be due to the thermally grown oxides on the surfaces.

The DSC curves shown in Fig. 6(d) demonstrate the heat flow characteristics of the fabricated thin films. A steady linear increase of heat flow was observed starting from -1mW to 0.13 mW and 0.24 mW for ATN and FATN, respectively, while the temperature increased from 100 °C to 630 °C. An endothermic peak was observed at around 635 °C, after which the heat flow started to drop sharply and reached -1.35 mW and -0.75 mW at 685 °C for ATN and FATN, respectively. The sudden drop in heat flow can be predicted as the melting of Al of the samples as the melting temperature of Al is around 660–670 °C. It can be deduced from these analyses that both TFMGs show excellent thermal stability over a broad range of temperatures. Hence, ATN and FATN thin films can be potential candidates as coatings to protect the base materials in hot environment observed in oil and gas industries.

4. Conclusion

In summary, two thin-film metallic glasses, ATN and FATN, have been fabricated using magnetron sputtering technique. The XRD of both ATN and FATN thin films exhibited amorphous microstructure, while the

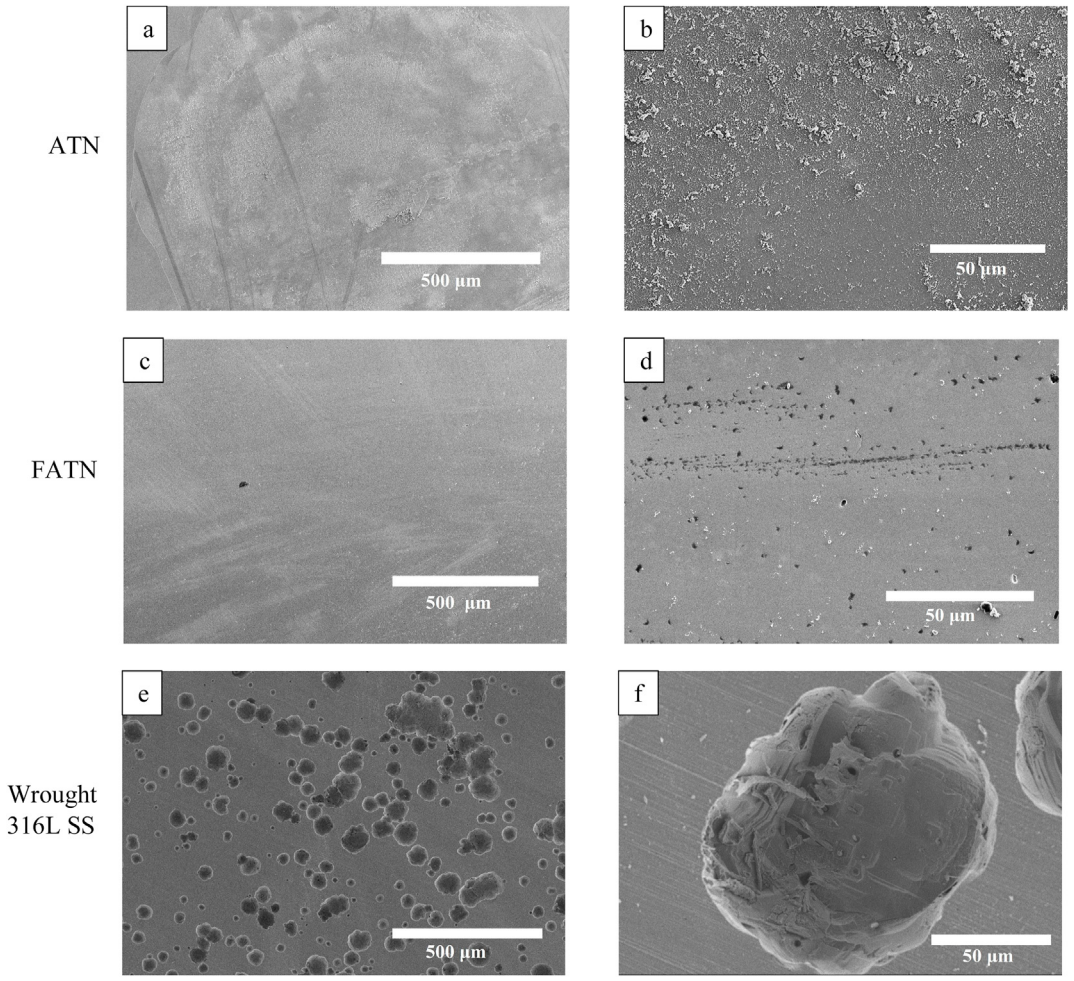

Fig. 5. Surface morphology of corroded samples after potentiodynamic polarization tests in 1 M NH_4Cl+1 M $Na_2S_2O_3$ solution. (a & b) ATN thin film, (c & d) FATN thin film, and (e & f) wrought 316L SS.

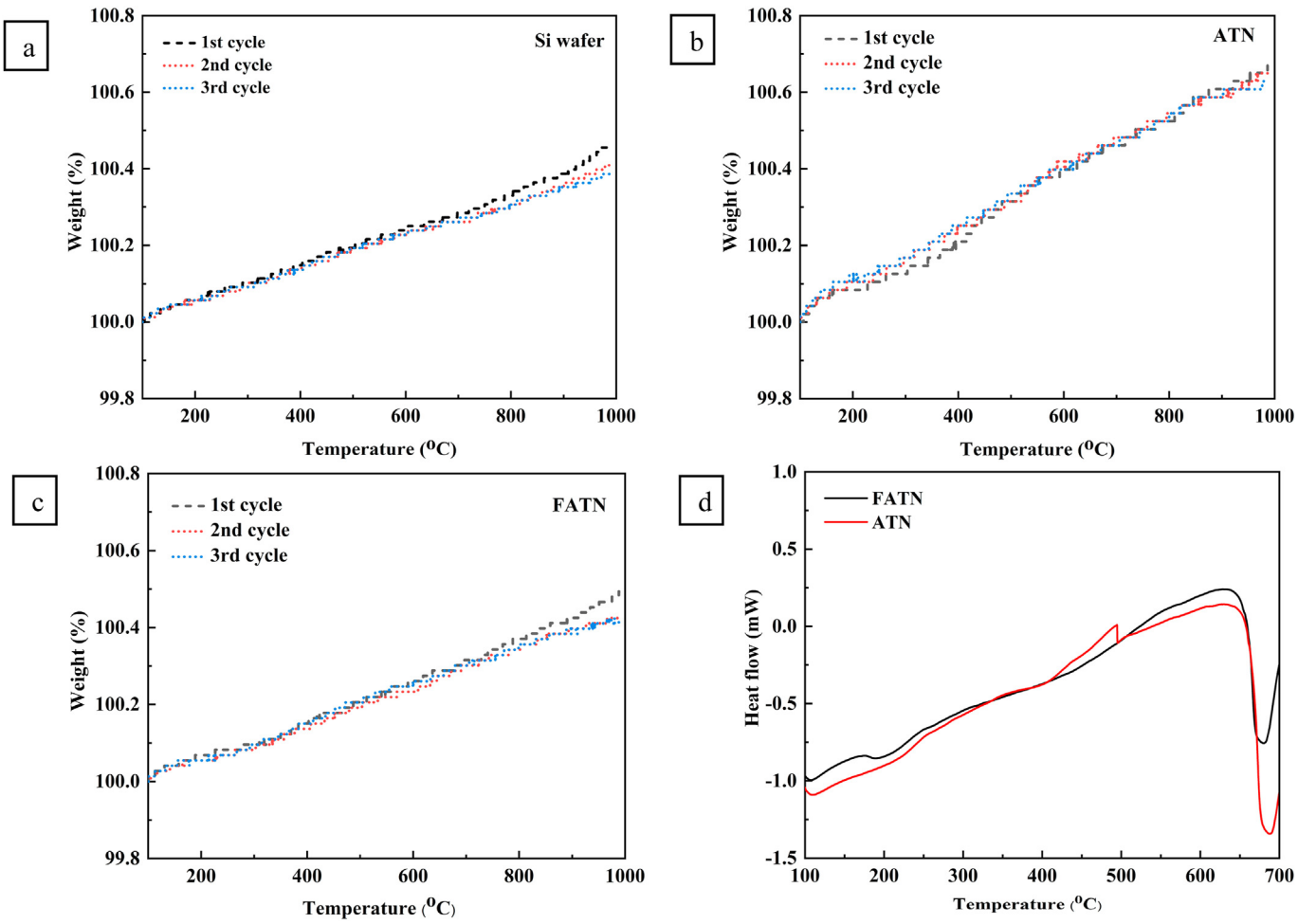

Fig. 6. TGA curves of (a) Si wafer, (b) ATN film, and (c) FATN film. (d) DSC curves of ATN and FATN thin films.

wrought sample showed a crystalline structure. XPS of the TFMGs manifests the presence of oxide film on the ATN and FATN surface, predominantly comprised of Al_2O_3, FeO/Fe_2O_3, TiO_2. Their corrosion performance has been evaluated and compared with wrought 316L SS in 1 M NH_4Cl+1 M $Na_2S_2O_3$ solution simulating the corrosive atmosphere of oil and gas industries. The TFMGs show superior corrosion resistance compared to wrought 316L SS in terms of lower corrosion current density, lower passivation current density, higher breakdown potential, higher charge transfer resistance, higher film resistance, and lower capacitance values. CV results show better passive film stability of the TFMGs and less susceptibility to pitting corrosion than the wrought sample, which is also evident from the post-corrosion surface morphology. The enhanced corrosion resistance of TFMGs can be attributed to the oxide layer formation on the surface and the amorphous microstructure of the films. Finally, no weight loss up to 1000 °C and higher melting temperatures as observed in TGA and DSC curves, respectively, indicate higher thermal stability of the fabricated thin films in hot environment. Overall, the rigorous electrochemical and microstructural analyses indicate the potential of the fabricated thin-film metallic glass coatings in oil and gas industries due to their outstanding corrosion resistance characteristics.

Declaration of competing interest

The authors declare that they have no known competing financial interests or personal relationships that could have appeared to influence the work reported in this paper.

Acknowledgement

The authors would like to acknowledge the College of Science and Engineering of Central Michigan University for financial support.

References

[1] M. Askari, M. Aliofkhazraei, S. Ghaffari, A. Hajizadeh, J. Nat. Gas Sci. Eng. 58 (2018) 92–114, https://doi.org/10.1016/j.jngse.2018.07.025.
[2] M. Iannuzzi, A. Barnoush, R. Johnsen, Npj Mater. Degrad. 1 (2017), https://doi.org/10.1038/s41529-017-0003-4.
[3] N.S. Al-Mamun, W. Haider, I. Shabib, Electrochim. Acta 362 (2020), 137039, https://doi.org/10.1016/j.electacta.2020.137039.
[4] F.F. Eliyan, F. Mohammadi, A. Alfantazi, Corrosion Sci. 64 (2012) 37–43, https://doi.org/10.1016/j.corsci.2012.06.032.
[5] S. Freitas, M.M. Malacarne, W. Romão, G.P. Dalmaschio, E.V.R. Castro, V.G. Celante, M.B.J.G. Freitas, Fuel 104 (2013) 656–663, https://doi.org/10.1016/j.fuel.2012.05.003.
[6] A. Davoodi, M. Pakshir, M. Babaiee, G.R. Ebrahimi, Corrosion Sci. 53 (2011) 399–408, https://doi.org/10.1016/j.corsci.2010.09.050.
[7] H. Luo, C.F. Dong, K. Xiao, X.G. Li, Appl. Surf. Sci. 258 (2011) 631–639, https://doi.org/10.1016/j.apsusc.2011.06.077.
[8] M. Kappes, G.S. Frankel, N. Sridhar, R.M. Carranza, J. Electrochem. Soc. 159 (2012) C195–C204, https://doi.org/10.1149/2.085204jes.
[9] H.S. Kuo, H. Chang, W.T. Tsai, Corrosion Sci. 41 (1999) 669–684, https://doi.org/10.1016/S0010-938X(98)00137-1.
[10] P.R. Roberge, S. Wang, R. Roberge, Mater. Org. (Berl.) 52 (1996) 733–737.
[11] K. Toba, K. Kawano, J. Sakai, NACE - Int. Corros. Conf. Ser. 68 (2014) 1049–1056.
[12] H. Ezuber, A. Alshater, M. Abulhasan, Surf. Eng. Appl. Electrochem. 53 (2017) 493–500, https://doi.org/10.3103/S1068375517050052.
[13] B. Matthes, E. Broszeit, J. Aromaa, H. Ronkainen, S.P. Hannula, A. Leyland, A. Matthews, Surf. Coating. Technol. 49 (1991) 489–495, https://doi.org/10.1016/0257-8972(91)90105-6.
[14] P.J. Kelly, R.D. Arnell, Vacuum 56 (2000) 159–172, https://doi.org/10.1016/S0042-207X(99)00189-X.

[15] C.L. Chang, F.C. Yang, Surf. Coating. Technol. 352 (2018) 330–337, https://doi.org/10.1016/j.surfcoat.2018.08.023.
[16] R.M. Fonseca, R.B. Soares, R.G. Carvalho, E.K. Tentardini, V.F.C. Lins, M.M.R. Castro, Surf. Coating. Technol. 378 (2019), 124987, https://doi.org/10.1016/j.surfcoat.2019.124987.
[17] L. Cunha, M. Andritschky, L. Rebouta, K. Pischow, Surf. Coating. Technol. 116–119 (1999) 1152–1160, https://doi.org/10.1016/S0257-8972(99)00270-4.
[18] G.X. Shen, Y.C. Chen, C.J. Lin, Thin Solid Films 489 (2005) 130–136, https://doi.org/10.1016/j.tsf.2005.05.016.
[19] E. Marin, A. Lanzutti, M. Lekka, L. Guzman, W. Ensinger, L. Fedrizzi, Surf. Coating. Technol. 211 (2012) 84–88, https://doi.org/10.1016/j.surfcoat.2011.08.026.
[20] M. Akhtari Zavareh, A.A.D.M. Sarhan, R. Karimzadeh, R.S.A./.K. Singh, Ceram. Int. 44 (2018) 5967–5975, https://doi.org/10.1016/j.ceramint.2017.12.175.
[21] B. Huang, C. Zhang, G. Zhang, H. Liao, Surf. Coating. Technol. 377 (2019), 124896, https://doi.org/10.1016/j.surfcoat.2019.124896.
[22] S. Wang, Y. Li, X. Wang, S. Yamaura, W. Zhang, J. Non-Cryst. Solids 476 (2017) 75–80, https://doi.org/10.1016/j.jnoncrysol.2017.09.028.
[23] D.P. Wang, S.L. Wang, J.Q. Wang, Corrosion Sci. 59 (2012) 88–95, https://doi.org/10.1016/j.corsci.2012.02.017.
[24] A. Lindsay Greer, Nature 366 (1993) 303–304.
[25] A. Inoue, Acta Mater. 48 (2000) 279–306, https://doi.org/10.1016/S1359-6454(99)00300-6.
[26] A.P. Grosvenor, B.A. Kobe, M.C. Biesinger, N.S. McIntyre, Surf. Interface Anal. 36 (2004) 1564–1574, https://doi.org/10.1002/sia.1984.
[27] M. Muhler, R. Schlögl, G. Ertl, J. Catal. 138 (1992) 413–444, https://doi.org/10.1016/0021-9517(92)90295-S.
[28] J.K. Parle, A. Beni, V.R. Dhanak, J.A. Smerdon, P. Schmutz, M. Wardé, M.G. Barthés-Labrousse, B. Bauer, P. Gille, H.R. Sharma, R. McGrath, Appl. Surf. Sci. 283 (2013) 276–282, https://doi.org/10.1016/j.apsusc.2013.06.101.
[29] K. Idczak, R. Idczak, R. Konieczny, Phys. B Condens. Matter 491 (2016) 37–45, https://doi.org/10.1016/j.physb.2016.03.018.
[30] B. Bharti, S. Kumar, H.N. Lee, R. Kumar, Sci. Rep. 6 (2016) 1–12, https://doi.org/10.1038/srep32355.
[31] S. Oktay, Z. Kahraman, M. Urgen, K. Kazmanli, Appl. Surf. Sci. 328 (2015) 255–261, https://doi.org/10.1016/j.apsusc.2014.12.023.
[32] M.M. Khan, K.M. Deen, W. Haider, J. Non-Cryst. Solids 523 (2019), 119544, https://doi.org/10.1016/j.jnoncrysol.2019.119544.
[33] J.L. Ke, C.H. Huang, Y.H. Chen, W.Y. Tsai, T.Y. Wei, J.C. Huang, Appl. Surf. Sci. 322 (2014) 41–46, https://doi.org/10.1016/j.apsusc.2014.09.204.
[34] C.L. Qiu, Q. Chen, L. Liu, K.C. Chan, J.X. Zhou, P.P. Chen, S.M. Zhang, Scripta Mater. 55 (2006) 605–608, https://doi.org/10.1016/j.scriptamat.2006.06.018.
[35] M.J.K. Lodhi, K.M. Deen, M.C. Greenlee-Wacker, W. Haider, Addit. Manuf. 27 (2019) 8–19, https://doi.org/10.1016/j.addma.2019.02.005.
[36] S. Tian, K. Sun, H. Cui, X. Xie, X. Wang, N. Wei, H. Wang, W. Wang, X. Song, K. Yang, Thin Solid Films 692 (2019), 137640, https://doi.org/10.1016/j.tsf.2019.137640.
[37] F. Movassagh-Alanagh, M. Mahdavi, Surf. Interfaces 18 (2020), 100428, https://doi.org/10.1016/j.surfin.2019.100428.
[38] Z. Li, C. Zhang, L. Liu, J. Alloys Compd. 650 (2015) 127–135, https://doi.org/10.1016/j.jallcom.2015.07.256.
[39] A. Obeydavi, A. Shafyei, A. Rezaeian, P. Kameli, J.W. Lee, J. Non-Cryst. Solids 527 (2020), 119718, https://doi.org/10.1016/j.jnoncrysol.2019.119718.
[40] A.P. Wang, X.C. Chang, W.L. Hou, J.Q. Wang, Corrosion Sci. 49 (2007) 2628–2635, https://doi.org/10.1016/j.corsci.2006.12.017.
[41] J. Tang, L. Yu, J. Qiao, Y. Wang, H. Wang, M. Duan, M. Chamas, Electrochim. Acta 267 (2018) 222–233, https://doi.org/10.1016/j.electacta.2018.02.071.
[42] M. Kappes, G.S. Frankel, N. Sridhar, R.M. Carranza, Corrosion 68 (2012) 872–884, https://doi.org/10.5006/0610.
[43] H.M. Ezuber, Mater. Des. 30 (2009) 3420–3427, https://doi.org/10.1016/j.matdes.2009.03.028.
[44] G.T. Burstein, C. Liu, R.M. Souto, S.P. Vines, Corrosion Eng. Sci. Technol. (2004) 25–30, https://doi.org/10.1179/147842204225016859.
[45] P.M. Natishan, W.E. O'Grady, F.J. Martin, R.J. Rayne, H. Kahn, A.H. Heuer, J. Electrochem. Soc. 158 (2011) C7, https://doi.org/10.1149/1.3520000.
[46] W.P. Yang, D. Costa, P. Marcus, J. Electrochem. Soc. 141 (1994) 2669–2676, https://doi.org/10.1149/1.2059166.
[47] A. Igual Muñoz, J. García Antón, J.L. Guiñón, V. Pérez Herranz, Corrosion Sci. 48 (2006) 4127–4151, https://doi.org/10.1016/j.corsci.2006.03.009.
[48] D. Xia, S. Song, R. Zhu, Y. Behnamian, C. Shen, J. Wang, J. Luo, Y. Lu, S. Klimas, Electrochim. Acta 111 (2013) 510–525, https://doi.org/10.1016/j.electacta.2013.08.030.
[49] Y.E. Durmus, S.S. Montiel Guerrero, H. Tempel, F. Hausen, H. Kungl, R.A. Eichel, Front. Chem. 7 (2019) 1–13, https://doi.org/10.3389/fchem.2019.00800.
[50] D.D. Silva, L.C. Campanelli, L. Bergmann, J.F. dos Santos, P. Hammer, C.A.D. Rovere, J.M. Aquino, Electrochim. Acta 358 (2020), https://doi.org/10.1016/j.electacta.2020.136900.
[51] T. Piao, S. Park, J. Electrochem. Soc. 144 (1997) 3371–3377, https://doi.org/10.1149/1.1838021.
[52] D. Xia, S. Song, R. Zhu, Y. Behnamian, C. Shen, J. Wang, J. Luo, Y. Lu, S. Klimas, Electrochim. Acta 111 (2013) 510–525, https://doi.org/10.1016/j.electacta.2013.08.030.
[53] L. Choudhary, D.D. Macdonald, A. Alfantazi, Corrosion 71 (2015) 1147–1168, https://doi.org/10.5006/1709.
[54] P.K. Baranwal, P.V. Rajaraman, J. Mater. Res. Technol. 8 (2019) 1366–1378, https://doi.org/10.1016/j.jmrt.2018.05.029.
[55] J. Zhou, Y. Yang, M. Alonso Frank, R. Detsch, A.R. Boccaccini, S. Virtanen, ACS Appl. Mater. Interfaces 8 (2016) 26482–26492, https://doi.org/10.1021/acsami.6b07068.